

# Catalytic activity and chemical structure of Nano MoS2 synthesized in a controlled environment



Reaction Chemistry & Engineering

ARTICLE

# Catalytic activity and chemical structure of Nano $MoS_2$ synthesized in a controlled environment

Received 00th January 20xx,
Accepted 00th January 20xx

DOI: 10.1039/x0xx00000x

www.rsc.org/

H. Zhang,[a] H. Lin,[a] Y. Zheng[a,c]*, Y.F. Hu[b], A. MacLennan[b]

A novel hydrothermal method for preparation of nano $MoS_2$ for hydrodesulfurization (HDS) with $MoO_3$ as precursors is presented. The redox reaction mechanism is, for the first time, revealed. It is shown to involve the oxidation of $S^{2-}$ to $SO_4^{2-}$ while hexavalent Mo is reduced to quadrivalent Mo to form $MoS_2$. $HS^-$ group is identified to play a key role in reduction of $MoO_3$. The acid-base behaviour of $Na_2S$ to $HS^-$ group and the yield of the resulting $MoS_2$ are controlled via the pH of the synthesis solution. Various characterization methods, e.g. XRD, TEM, SEM, BET, TPR, XPS, XANES, EXAFS, etc. are employed for the characterization of the synthesized $MoS_2$. The results show that high purity $MoS_2$ is obtained. The ratio of precursors, $MoO_3$ and $Na_2S$, influences the crystal structure and catalytic activity. Slight less sulfur than stoichiometric ratio of S/Mo produces defect sites, which promotes catalyst activities in the hydrodesulfurization of real light cycle oil (LCO).

## Introduction

Nano-scaled molybdenum disulfide ($MoS_2$) has a layered structure with individual sheets strongly covalently bonded within but held together through weak van der Waals interactions. This results in two distinct surfaces of $MoS_2$: basal and edge planes. Within a layer, each Mo (IV) center is bonded to six sulfurs forming a trigon prismatic coordination while every sulfur atom is connected with three Mo forming pyramidal interstices[1,2]. The unique structure and chemistry properties make $MoS_2$ widely applied as a functional material in diverse fields of lubrication, electronic transistors, batteries, photovoltaics, catalysis, and sensing[3]. $MoS_2$ also shows high activity in hydrodesulfurization reaction[4].

There are different methods for synthesis of nano $MoS_2$ including solid-gas sulfidation, thermal decomposition, and solution reactions[5]. Hydrothermal method is an alternative route to preparing nano $MoS_2$ with $MoO_3$ as precursor[6]. Compared to thiomolybdate, $MoO_3$ is an attractive precursor as it is cost-effective. $MoO_3$ has been used as precursor to synthesize nano $MoS_2$ of different morphologies, e.g. nano-sheet[4], nanowires[7], nanotubes and nanorods[8]. Our previous study discussed the effect of temperature on the nucleation and growth process[6]. A relationship has been established between the crystallization process and $MoS_2$ structure. Successful production of nano $MoS_2$ through hydrothermal route is associated with a number of synthesis parameters such as pH of solvent, precursor concentration, and temperature. However the reaction mechanisms for formation of $MoS_2$ are poorly understood.

This work tends to address this deficiency. In particular, the role of reducing agent in transformation of hexavalent Mo to quadrivalent Mo to form $MoS_2$ will be studied. The reaction mechanism of the nano $MoS_2$ formation is discussed. Appropriate synthesis condition results in high yield of highly dispersed nano $MoS_2$ crystalline that has high hydrodesulfurization activity. The textural and chemical structure of synthesized catalysts were extensively characterized by various techniques, e.g. TEM, BET, XRD, XPS, TPR and XAFS, etc. The hydrodesulfurization (HDS), hydrodenitrogenation (HDN) activities were evaluated using a real diesel fraction - light cycle oil (LCO).

## Experimental Section

**Preparation of $MoS_2$ catalysts.** A series of molybdenum sulfide catalysts were synthesized using $MoO_3$ (STEM Scientific) and $Na_2S{\cdot}9H_2O$ (Fisher Scientific) as precursors[6]. 14.4 grams of $MoO_3$ was used in the synthesis. Different molar ratios of $Na_2S$ to $MoO_3$ were employed and listed in Table 1. $Na_2S{\cdot}9H_2O$ and $MoO_3$ were gradually dissolved in deionized water and 4M HCl was added drop-wisely to adjust the pH of the solution. The mixture was then transferred into autoclave and reacted for 2 h at 320˚C at 500 rpm in nitrogen or hydrogen atmospheres. The resultant black solid was filtered, washed using deionized water and ethanol, and then dried under nitrogen protection at 150 ˚C for 4 h. The catalyst recovery rate was calculated based on theoretical $MoS_2$ yield (Equation 1). The prepared $MoS_2$ catalysts at various $Na_2S$ to $MoO_3$ molar ratios were denoted as CAT–x (where x stands for the molar ratio of $Na_2S$ to $MoO_3$). pH values of the initial synthesis solution and the final filtrate were determined using a pH meter (AB 15, Fisher Scientific). The concentrations of sulfur anions $S_2O_3^{2-}$ and $SO_4^{2-}$ in the filtrate

[a] University of New Brunswick, 15 Dineen Dr. Fredericton, NB, E3B 5A3Canada.
[b] Canadian Lightsource Inc. 44 Innovation Blvd, Saskatoon, SK S7N 2V3 Canada
[c] University of Edinburgh, Mayfield Road, Edinburgh, EH9 3DW, UK

were determined by an ion chromatography (DIONEX, DX-120). The reference $MoS_2$ was purchased from SPI supplies.

$$\text{Recovery} = \frac{\text{Actual W}_{MoS_2}}{Theorectical W_{MoS_2}} \times 100\% \quad \text{Equation 1}$$

**Catalyst characterization.** The transmission electron microscopic (TEM) images were recorded on a JEOL 2011 STEM (JEOL Ltd., Tokyo, Japan) operated under high-resolution mode and 200 keV electronical energy. The average length and thickness of $MoS_2$ crystals calculated using Equations 2 and 3 were expected values. At least 200 images of different $MoS_2$ particles (particle' refers to one MoS2 crystalline) were used. The morphology of catalysts was also observed by Scanning electron microscopy (JEOL JSM6400 SEM).

$$\textit{Average thickness } \bar{T} = \frac{\sum_{i=1,2,\ldots} N_i T_i}{\sum_{i=1,2,\ldots} N_i} = \frac{\sum_{i=1,2,\ldots} N_i T_i}{N} \quad \text{Equation 2}$$

$$\text{Average length } \bar{L} = \frac{\sum_{i=1,2,\ldots} N_i L_i}{\sum_{i=1,2,\ldots} N_i} = \frac{\sum_{i=1,2,\ldots} N_i L_i}{N} \quad \text{Equation 3}$$

where *T*, *L*, and *i* stand for thickness, length, and number of layers , respectively. $\bar{T}$ is the expected value of particle thickness and $\bar{L}$ is the expected value of particle length. It is assumed that all i-th layered particles have the same thickness ($T_i$). The length of i-th layered particles, $L_i$, is an average length of the particles that have the same numbers of layers (i). $N_i$ denotes the number of i-th layered particles and N represents the total number of particles.

The measurement of nitrogen adsorption-desorption isotherm was conducted on Autosorb-1 (Quantachrome Instruments). The specific surface area of catalyst was determined using the Brunauer-Emmett-Teller (BET) method. The total pore volume was calculated from the volume of nitrogen adsorbed at the relative pressure $p/p_0$ 0.995. Pore size distribution was analyzed from the isotherms by the Barrett-Joyner-Halenda (BJH) method.

The synthesized products were identified by the X-ray diffraction (XRD) pattern, which were recorded on a diffractometer (Bruker AXS D8 XRD) using Cu*Kα* radiation with the 2θ range of 5-85° and the scan speed of 1°/min.

The elemental analysis for molybdenum and sulfur was conducted on a JEOL-733 Superprobe, operating at 15 keV and 100 nA.

Temperature programmed reduction (TPR) was conducted on Autosorb-1 (Quantachrome Instruments). 100 mg catalyst was added in a quartz tube and heated to 700°C at a rate of 10°C/min, under a 50 ml/min flow of 2% $H_2$ in Ar. The consumption of $H_2$ and production of $H_2S$ was monitored by a mass spectrometer (RGA 200 Stanford Research Systems, Inc.).

The XPS measurements were performed on an AXIS 165 spectrometer (Kratos Analytical, University of Alberta). The base pressure in the analytical chamber was lower than 3 x $10^{-8}$ Pa. Monochromatic Al Kα source (hv = 1486.6 eV) was used at a power of 210 W. The analysis spot was 400 ×700 µm. The resolution of the instrument is 0.55 eV for Ag 3d and 0.70 eV for Au 4f peaks. The survey scans were collected for binding energy extending from 1100 eV to 0 with pass energy of 160 eV and a step of 0.4 eV. 20 eV with a step of 0.1 eV was used for the pass-energy for high-resolution spectra. The number of scans varied from 3 to 30 to ensure a good signal to noise ratio.

The X-ray absorption near edge structure (XANES) spectra were obtained at a Soft X-ray Microanalysis Beamline (SXRMB) of the Canadian Light Source (CLS; Saskatoon, SK, Canada) equipped with a Si (1 1 1) double crystal monochromator. CLS, a 2.9 GeV, third generation storage ring, presently operates with an injection current of 250 mA. Samples were sulfided at 280˚C in $H_2$ with dimethyl disulfide (DMDS) for 2h prior to measurement. Catalyst powders were uniformly dispersed on double-sided conducting carbon tapes under a dry nitrogen atmosphere. The measurements of S K-edge and Mo $L_3$-edge were made in total electron yield by recording the sample drain current. Data analysis of the XANES spectra was performed using Athena software. Mo K-edge EXAFS spectra were recorded in the transmission mode at room temperature. Fourier transformation of the k/f (k) weighted EXAFS data for $\Delta k=14 Å^{-1}$($3<k<17$) was performed to obtain the radial distribution function around Mo. Detailed procedure was described elsewhere[8].

**Hydrodesulfurization evaluation**. A batch reactor (Parker Autoclave Engineers) was employed in this experiment. A light cycle oil (LCO) with 1.46% S and 156 ppm N provided by a local refinery was used as feedstock. When the reactor was heated to 375 ºC, LCO was introduced into the reactor. The weight ratio of catalyst to oil is 1:200. The hydrodesulfurization (HDS) and hydrodenitrogenation (HDN) took place at 375 ºC under $H_2$ gas pressure of 1400-1500 psi and 1000 rpm.

The total sulfur and nitrogen concentrations of the feedstock and the hydrotreated products were measured by a Sulfur/Nitrogen analyzer (9000 series, Antek Instruments Inc). The sulfur species were analyzed by a gas chromatography (GC) equipped with a non-polar VF-1ms capillary column (15 m x 0.25 mm x 0.25 µm, max temperature: 325°C) and a PFPD detector (Varian 450). The following temperature profile was used: 2 min at 120°C, followed by a linear increase at 6°C /min to 170°C and a further increase at 20°C /min to 290°C, kept for 2 min. Density of the liquid oil was measured by a portable density meter (DMA 35N, Anton Paar GmbH, Graz, Austria) following ASTM 4052. The HDS/HDN conversion was calculated by subtracting the sulfur/nitrogen in the feed from product and divided by the sulfur/nitrogen in the feed. The calculation of rate constant k was based on pseudo-first order reaction.

## Results and discussion

**Synthesis of $MoS_2$ in controlled medium.** A series of $MoS_2$ were synthesized in a medium of controlled pH values. The experimental parameters are shown in Table 1. $MoO_3$ and $Na_2S$ serve as molybdenum and sulfur sources, respectively. Without addition of HCl, precursor $Na_2S$ is first mixed in deionized water. Then $MoO_3$ powders were slowly stirred in and completely dissolved in the

 

basic solution. A clear yellow liquid with pH=12.59 was resulted, which liquid was then transferred to an autoclave for 2 hour hydrothermal reaction at 320˚C. No solid catalyst was produced (entry 1). HCl was used to adjust the pH of resulted liquid mixture for all other entries. The clear yellow liquid turns to be dark red or brown once HCl was dropped in. Slightly reducing initial pH of the $Na_2S$-$MoO_3$ solution from 12.59 to 10.61, a small amount of dark solid product was detected after the 2-hour synthesis (entry 2). The single 002 diffraction peak shown in the XRD pattern (Figure 1) confirmed that the solid product was amorphous $MoS_x$. Continuous adjustment of the $Na_2S$-$MoO_3$ solution to pH=5.70 (entry 3) leads to a satisfactory result. The yield of $MoS_2$ reached as high as 96% of its theoretical value. The obtained $MoS_2$ also shows satisfactory crystallinity as indicated by the XRD pattern (Figure 1). Further acidification of the $Na_2S$-$MoO_3$ solution to pH=0.95 lead to an unsuccessful synthesis (entry 4) with significant amount of $MoO_2$ identified. This finding suggests that the initial pH of synthesis solution plays a key role in formation of nano crystalline $MoS_2$.

Gaseous environment is also a factor that influences the conversion from $MoO_3$ to $MoS_2$. With inert gas (nitrogen) filled in the reaction chamber, $Na_2S$ ($S^{2-}$) acted as reduction agent and crystallized $MoS_2$ was successfully synthesized (entry 3, 5 and 6). However, reductive gas, e.g. hydrogen gas, can replace $Na_2S$, function as a reduction agent during the synthesis, reducing $MoO_3$ to $MoO_2$ instead of formation of $MoS_2$ (Figure 1). Compared to entries 5 & 6, entry 7 has a very high pH of filtrate suggests little comsumption of $Na_2S$ during the synthesis (Table 1). Reductive gas atmosphere has negative impact on the formation of crytallized $MoS_2$**.**

**Synthesis reactions: identification of the key role of $H^+$ and $HS^-$.** In the hydrothermal synthesis, crystalline $MoS_2$ is formed from the redox reaction of $MoO_3$ and $Na_2S$, where Mo is reduced from $Mo^{6+}$ to $Mo^{4+}$. Sodium sulfide is hydrolyzed in water to give strong alkaline solutions, as shown in Reaction 1 and Reaction 2. Due to acid nature, $MoO_3$ is easily dissolved in the basic solution to give $MoO_4^{2-}$ (Reaction 3), forming a clear yellow solution, as seen in entry 1 of Table 1. Unfortunately, $MoO_4^{2-}$ group is not directly responsible for the precipitation of solid $MoS_2$.

$$S^{2-} + H_2O \leftrightarrow HS^- + OH^- \quad \text{Reaction 1}$$

$$HS^- + H_2O \leftrightarrow H_2S + OH^- \quad \text{Reaction 2}$$

$$MoO_3 + 2OH^- \leftrightarrow MoO_4^{2-} + H_2O \quad \text{Reaction 3}$$

$$MoO_4^{2-} + nH^+ + nHS^- \leftrightarrow MoO_{4-n}S_n^{2-} + nH_2O \quad (n=1\text{-}4) \quad \text{Reaction 4}$$

$$MoS_4^{2-} + H^+ \leftrightarrow MoS_3\downarrow + HS^- \quad \text{Reaction 5}$$

$$MoS_3 \xrightarrow[\Delta]{} MoS_2 + S \quad \text{Reaction 6}$$

$$4S + 3H_2O \xrightarrow[\Delta]{} 4H^+ + 2HS^- + S_2O_3^{2-} \quad \text{Reaction 7}$$

$$S_2O_3^{2-} + H_2O \xrightarrow{\Delta,\ H^+} SO_4^{2-} + H^+ + HS^- \quad \text{Reaction 8}$$

Addition of a few drops of HCl darkens the solution. Continuous titration of acids leads to precipitation of solids (entry 2), which is confirmed to be molybdenum sulfides (amorphous). $H^+$ appears to be a likely mechanistic requirement for the solid precipitation. It is known that $MoO_4^{2-}$ could react with $H^+$ and $HS^-$ to form tetrahedral sulfido-molybdenum complexes such as $MoOS_3^{2-}$, $MoO_2S_2^{2-}$, $MoO_3S^{2-}$ and $MoS_4^{2-}$ [10]. This is a $[H^+]$-dependent process and high $[H^+]$ is beneficial to O removal. The $HS^-$ was confirmed to be an effective incoming nucleophile to interact with $O^{2-}$ on Mo (VI) [10]. Sufficient $[H^+]$ and $[HS^-]$ is then led to initial precipitation of $MoS_x$ at room temperature [5], which is the seed for production of crystal $MoS_2$ [7]. Reaction 4 and Reaction 5 are proposed to describe the process.

$HS^-$ group plays a key role in the redox reaction. The hydrolysis of sulfide ion gives three species: $S^{2-}$, $HS^-$ and $H_2S$. Given the ΔH and ΔG[16], rate constants can be calculated and then the molar concentrations of the three species at different pH can be determined. The theoretical acid-base behaviour of the $S^{2-}$, $HS^-$ and $H_2S$ as a function of pH are shown in Figure 2. In strong alkaline solutions, sulfide ion presents in the deprotonated form as the sulfide dianion, $S^{2-}$ while in strong acid environment, it exists in the form of $H_2S$. $HS^-$ becomes inadequate in both strong acid and strong alkaline synthesis solution. Without sufficient $HS^-$ Reaction 4 most likely stops and thus formation of intermediate complexes $MoO_{4-n}S_n^{2-}$ becomes limited. The presence of $S^{2-}$ in strong alkaline solution cannot facilitate Reaction 4 to proceed (entry 2). This suggests that $S^{2-}$ plays no role in formation of $MoS_2$. With strong acid solution, large amount of $H_2S$ produced and remains in gaseous phase due to its poor solubility in acidic solution. A certain amount of $MoO_2$ is formed (entry 4). On the other hand, $HS^-$ is produced in mild acid solution (entry 3, 5 and 6) and good yields of $MoS_2$ are obtained. Therefore, the formation and the production yield of crystalline $MoS_2$ is highly associated with $[H^+]$ and $[HS^-]$. Both insufficient $[H^+]$ and overdose $[H^+]$ generate inappropriate pH of the synthesis solution, which results in unsatisfactory concentration of $HS^-$ and then little $MoS_2$ can be produced. Species $HS^-$ presents in neutral and basic solutions at room temperature. The pH for $HS^-$ group shifts to lower values at the hydrothermal synthesis temperature, 320°C, with an optimal range falling between 6 and 8. It is fair to comment that formation of $MoS_2$ is a $[H^+]$ and $[HS^-]$ dependent process. Up to this point, it seems that both weak acid and basic initial solutions are suitable for $MoS_2$ synthesis. A further discussion presents below to interpret whether mild acid or mild basic solution is optimal for the production of $MoS_2$.

At synthesis temperature, 320°C, the precipitated solid $MoS_3$ from Reaction 5 is reduced to $MoS_2$ companying by production of sulfur element in Reaction 6 (Sulfur element was observed in the synthesis). Sulfur element reacts with water to $S_2O_3^{2-}$ which may be further oxidized to $SO_4^{2-}$. Reaction 7 and 8 are proposed. It is worth mentioning that $H^+$ and $HS^-$ are released in both redox Reactions. Generation of $HS^-$ directly enhances the precipitation of $MoS_3$ that is further reduced to $MoS_2$. Produced $H^+$ lowers the pH value of final filtrate than its initial solution. Apparently, complete oxidization of sulfur to $SO_4^{2-}$ favors high yield of $MoS_2$. $S_2O_3^{2-}$ is more stable in basic aqueous solution than acid solution. $S_2O_3^{2-}$ tends to be

oxidized to $SO_4^{2-}$ in acidic solution. Two catalysts, named CAT-2.5 and CAT-3.0 (Table 2) were synthesized at weak acid and weak basic initial solutions. 96.2% and 55.1% of the theoretical yield were obtained respectively. Concentration of $SO_4^{2-}$ in the filtrates directly corresponds to the $MoS_2$ yield. This demonstrates that initial synthesis solution must be weak acid to achieve optimal yield of $MoS_2$. A reaction scheme for hydrothermal synthesis of $MoS_2$ using $MoO_3$ and $Na_2S$ as precursors is summarized and shown in Scheme 1. The overall reactions are shown in Reaction 9 and Reaction 10 with $S_2O_3^{2-}$ and $SO_4^{2-}$ as main oxidized product, respectively.

**Adjustment of S/Mo ratio.** Six atomic ratios of sulfur to molybdenum of the precursors, ranging from 2 to 5, are prepared and the results are shown in Table 2. The stoichimetric S/Mo molar ratio in $MoS_2$ is 2. Since a portion of $Na_2S$ acts as redox mediator during the synthesis, the S/Mo ratios of the obtained $MoS_2$ are inevitably lower than its corresponding S/Mo ratios of precursors. Under-dosed $Na_2S$ inevitably leads to excessive $MoO_3$ in the synthesis, e.g. CAT-2.0. Molybdenum-dominant solid particles are generated and embedded between the layered $MoS_2$, resulting in poor uniformity of $MoS_2$ (Figure 3). On the other hand, excessive $Na_2S$ results in strong alkaline synthesis solution and thus scarce solid catalyst is formed, e.g. CAT-5.0. The XRD patterns and electron diffraction rings of the four catalysts, as shown (Figures 4 and 5), confirm the successful synthesis of $MoS_2$.

$$4MoO_3 + 9Na_2S + 16HCl \rightarrow 4MoS_2 + Na_2SO_4 + 16NaCl + 8H_2O \quad \text{Reaction 9}$$

$$4MoO_3 + 10Na_2S + 18HCl \rightarrow 4MoS_2 + Na_2S_2O_3 + 18NaCl + 9H_2O \quad \text{Reaction 10}$$

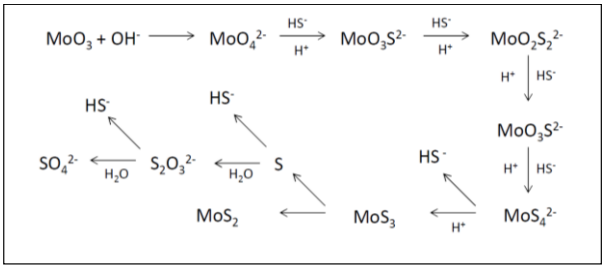


Scheme 1. Proposed reaction scheme for synthesis of $MoS_2$

**Determination of $MoS_2$ chemical structure.** Their S/Mo ratios of three catalysts, CAT-2.5, CAT-3.0, and CAT-3.75 determined by microprobe analysis are 1.85, 2.05 and 2.10, respectively (Table 3). The bulk and surface chemical states of the catalysts are identified by XANES and XPS spectra. The S K-edge (a) and Mo $L_3$-edge (b) XANES spectra are displayed in Figure 6. The spectra acquired simultaneously in total electron yield (TEY) with an estimated 100 nm in probing depth are more bulk sensitive. The peak (whiteline) at 2471eV (peak A) is due to the S 1s to 3p dominated transitions of S in -2 oxidation state[11]. According to the typical periodic slab model[12], two types of S coordination are noticed on the $MoS_2$ surface. Thus, two broad peaks (B and C) located at 2478-2484eV and 2489-2495eV may be attributed to S pyramidal coordination on basal planes and S hexogen structure, respectively. The Mo $L_3$-edge (whiteline) observed at 2524eV with the shoulder peak (2532eV) is associated with the electron transition from Mo $2p_{3/2}$ to vacant 4d [13, 14] and the trigonal prismatic coordination of Mo atoms, respectively [13, 15]. Apparently, all spectra exhibit identical vacancy state as the reference, indicating a high purity of $MoS_2$.

Typical XPS spectra of S 2p core level region of as-prepared $MoS_2$ catalysts are shown in Figure 7. All the spectra exhibit typical profiles of pure $MoS_2$ with strong S and Mo peaks. The S 2p spectra contain the S $2p_{3/2}$ (161.8 eV) and the S $2p_{1/2}$ (163.0 eV) spin-orbit doublet with intensity ratio of around 2:1, which are indexed to a typical spectrum of sulfide $S^{2-}$ ion[17]. Small but unmistakable differences in chemical shift are also observed among the catalysts. S $2p_{3/2}$ peak of CAT-2.5 slightly shifts to lower energy, whereas the peak of CAT-3.0 shifts to higher energy (circled), giving the electron binding energy order of CAT-2.5< CAT-3.75comple< CAT-3.0.

The TPR traces of sulfide catalysts are shown in Figure 8, illustrating the consumption of $H_2$ and the production of $H_2S$ in the temperature range of 100-500°C. For $H_2$ consumption, typical peaks for weakly bonded sulfur are observed in the low temperature range of 200-370°C. It is commonly accepted that the consumption of $H_2$ can reflect the number of weakly bonded sulfur on the surface of catalysts [12, 18]. $H_2$ is firstly dissociative adsorbed on two sulfur dimers which are bonded on adjacent Mo sites, creating two S-Mo-SH groups. Then one hydrogen atom transfers from one group to another to form a SH-Mo-SH group. Finally, $H_2S$ is released from an active site of *-Mo-S, where * refers to the sulfur vacancy [12]. However, one assumption is made that the two sulfur dimers bonded on the same Mo atom. Otherwise, the SH-Mo-SH group cannot be formed properly, in which case, the system needs to be stabilized by a state of two *-Mo-SH groups, thus, no $H_2S$ can be released. Therefore, the difference between $H_2$ consumption and $H_2S$ production in the TPR spectrum may differentiate the existing active sites from those that can be potentially formed. For catalyst CAT-2.5, the TPR spectrum shows a large $H_2$ consumption but no $H_2S$ production. The absence of a $H_2S$ peak suggests a high deficiency of S on the surface. The wide peak also suggests inhomogeneous defect sites. For the CAT-3.0 and CAT-3.75, the $H_2S$ content is highly associated with the $H_2$ consumption, indicating the high coverage of S on the surface. It is noted from the TPR spectra that the initiation temperature for releasing $H_2S$ is lower on CAT-3.75 than CAT-3.0 and the $H_2S$ curve is wider. This may be due to the different type of sulfur on the catalyst surface. CAT-3.75 contains over-stoichiometric sulfur that may be weakly bonded to catalyst thus easy to eliminate. In contrast, $H_2S$ curve over CAT-3.0 barely has none-stoichiometric sulfur. Sulfur species are uniformly bonded within CAT-3.0 so that $H_2S$ peak is sharp.

Figure 9 shows the Fourier transform of the Mo K absorption edge for all the three catalysts. The spectra show two notable peaks corresponding to Mo-S (peak A) and Mo-Mo (peak B)[15]. The first largest peak at 1.90Å (phase shift uncorrected) arises from sulfur atoms in the first coordination sphere around Mo atoms, while the second peak at 2.86Å (phase shift uncorrected) is due to the nearest neighbor Mo atoms. The EXAFS results exhibit a similar $MoS_2$ structure. The only difference noticed is that the Mo-Mo bond for CAT-2.5 is lower than the other two catalysts. The calculated coordination number (CN) from the Fourier transform is shown in

Table 4. It is noticed that all the three catalysts exhibit lower CN than the $MoS_2$ in bulk. Similar to the spectra, the smallest CN of Mo-Mo is observed with CAT-2.5, indicating more disordered matrix on the surface.

**Characterization of textural structure.** The morphologies of the three catalysts with different S/Mo molar ratios are revealed by TEM (Error! Reference source not found.10). The dark thread-like lines shown in the fringes are the reflection of (0 0 2) lattice plane of the crystalline $MoS_2$, representing the stacked slabs. All the catalysts show dendritic morphologies and layered nanocrystallines. A large number of curved slabs are observed on the catalysts (circled in Figure 10), which may result in more defects created on the basal plane[20]. The three catalysts have similar size distributions. Table 3 shows narrow size ranges of 15.8-17.9 nm and 2.3-2.6nm, for the average slab length and thickness, respectively. The average lengths obtained in the present work are similar to the catalysts using $(NH_4)_2MoS_4$ (ATM) as precursors [20, 10] while are significantly shorter than the crystallized $MoS_2$ synthesized by Li et al. who reported 50 nm in length [8]. Figure 11 shows FE-SEM images of $MoS_2$. For both catalysts, thread-like $MoS_2$ crystals are associated in bundles and twisted together forming a flower-like morphology. The images exhibit nanosized particles with an average size of 100-200 nm. Mesopores over 10 nm are formed in between the crystals, as shown in the grey part surrounded by white $MoS_2$ layers. A slight difference observed is that CAT-2.5 looks more dendritic, while CAT-3.75 crystal favors growth on the boundary of particles.

The three catalysts have large surface area ranging from 200 to 262 $m^2/g$ (Table 3). A high pore volume of 0.9 to 2.3 $m^3/g$ is also observed, which is much higher than that of other catalysts previously reported[20].

**Catalytic activities.** Catalysts synthesized under hydrothermal method with $Na_2S$ and $MoO_3$ precursors are subjected to undergo a performance test on HDS, HDN, and hydrocracking activities, using LCO (Figures 12, 13 and 14). The initial HDS rate constants in the first hour for all catalysts are higher than $2\times10^{-4}$ $s^{-1}$ g $cata^{-1}$. The rates drop by half in the second hour and a further 50% off was observed in the rest of the reaction. The decrease of reaction rates for each catalyst along with reaction time is due to the fact that LCO contains both easy (benzothiophen and its derivatives) and hard sulfur (dibenzothiophen and its derivatives) compounds (Table 5). Nevertheless, it is still observable that CAT-2.5 presents the highest HDS activity and CAT-3.0 has the lowest activity. CAT-3.75 positions in between. CAT-2.5 also exhibits the highest HDN (Figure 12) and hydrocracking (seen from the product density in Figure14) ability.

The relationship between the properties and activities is plotted in Figure 15. The ratio of Mo atoms on edge to the total Mo atoms is calculated based on the slabs length, the method reported by Vrinat et. al.[22]. Apparently, if only Mo on the edges were active sites, the activity order would be totally opposite. It is indicated that the imperfect basal plane is important for the activities, and defects should be also largely located on the curved or twisted basal plane. This can be verified with TEM images; all the catalysts show highly curved morphologies. In particular, CAT-2.5 exhibits more blurred slabs, indicating more imperfect crystalline structure than the other two, which explains the highest activity of the three. There are also no clear relationship between activity and surface area (Figure 15 b). This statement has been mentioned by several researchers [21]. Certain surface area is essential to provide more accessible active sites, however, effect gets infinitesimal when sufficient exposed area are provided. Most of the calculated area is inert to the reaction.

As discussed in TPR, the hydrogen adsorbed is highly related to the active sites on the catalyst. From Figure 15 c, it's easy to see that there is a good linear relationship between the $H_2$ adsorption sites (Table 6) and HDS rate constant. The amount of active sites (as in $H_2$ reacted sites) reflects the catalyst activities. Similar phenomenon also can be seen from S/Mo atomic ratio macroscopically. The lack or excess of sulfur might be related to the deformation of the crystal structure and defects on the catalysts. When S/Mo ratio is lower than the stoichiometric atom ratio of $MoS_2$ (2), defect sites might be already generated due to the deficiency of S. On the other hand, over-stoichiometric sulfur may exist in the form of $S_2^{2-}$ species, which can react with $H_2$ to form –HS species and enhance hydrotreating reaction. As more defects are created during the synthesis, the $MoS_2$ would deviate further from the perfect crystal, in other words, S/Mo ratio would further deviate from the stoichiometric number 2. This is consistent with our results that $MoS_2$ has the highest difference with largest hydrogen adsorption sites. It is also showing excellent relationship between the difference and the activities, as in Figure 15 d.

Relationship also can be seen from binding energy, coordination, disorder and activities. Although the difference is not obvious, it's also found the binding energy and $MoS_2$ cluster size (reflected by Mo-Mo coordination number) show the similar trend of HDS activity.

## Conclusions

Novel nanocrystalline $MoS_2$ were successfully synthesized via hydrothermal method using commercially available $MoO_3$ and $Na_2S$. The synthesis mechanism of hydrothermal approach was investigated and the reaction pathways were proposed for the formation of crystalline $MoS_2$. $[HS^-]$ in the synthesis solution is identified as a key factor. Insufficient $[HS^-]$ can lead to a failure synthesis. Mild acidic medium is essential for a successful synthesis. The ratio of reactants, $MoO_3$ and $Na_2S$, is important to the nanocrystal structure and the yield. Excessive $MoO_3/Na_2S$ ratio may result in poor uniformity of $MoS_2$. Various characterization techniques are employed to assess the structure of synthesized catalysts. The three catalysts synthesized at the proper range of $Na_2S/MoO_3$ (from 2.5 to 3.75 in the work) have nanosized structure, large surface area, and high pore volume (mesopores). More defects at the rims are found on the CAT-2.5 than the other two catalysts. HDS activity of hydrotreating LCO also exhibits a decreasing order of CAT-2.5>CAT-3.75> CAT-3.0.

## Acknowledgements

The authors gratefully acknowledge the financial assistance from Canada Research Chairs program, the Natural Sciences and Engineering Research Council of Canada and the Canada Foundation for Innovation.

## References

1. R. Tenne, Angew. Chem. Int. Ed., 2003, **42**, 5124-5132.
2. R. Tenne, Nat Nano, 2006, **1**, 103-111.
3. X. Hu, W. Zhang, X. Liu, Y. Mei, Y. Huang, Chem. Soc. Rev., 2015, **44**, 2376-2404.
4. X. H. Zhang, H. Tang, M. Q. Xue, C. S. Li, Mater. Lett., 2014, **130**, 83-86.
5. Y. Araki, Y. Iwata, Y. Miki, K. Honna, N. Matsubayashi, H. Shimada, in: Hydrotreatment and Hydrocracking of Oil Fractions by B. Delmon, G.F. Froment, P. Grange (Eds.), Elsevier Science B.V., The Netherlands, 1999, pp. 69-76.
6. H. Zhang, H. Lin;Y. Zheng;Y. Hu;A. MacLennan Appl. Catal., B, 2015, 165, 537-546.
7. W.J. Li, E.W. Shi, J. M.Ko, Z.Z. Chen, H. Ogino, T. Fukuda, J. Cryst. Growth, 2003, **250**, 418-422.
8. Y. Tian, Y. He, J. Shang, Y.F. Zhu, Acta Chim Sinica, 2004, **62**, 1807-1810.
9. C. Calais, N. Matsubayashi, C. Geantet, Y. Yoshimura, H. Shimada, A. Nishijima, M. Lacroix, M. Breysse, J. Catal., 1998, **174**, 130-141.
10. B. Yoosuk, J.H. Kim, C. Song, C. Ngamcharussrivichai, P. Prasassarakich, CATAL TODAY, 2008, **130**, 14-23.
11. V. R. Surisetty, Y. F. Hu, A.K. Dalai, J. Kozinski, Appl. Catal., A, 2011, **392**, 166-172.
12. N. Dinter, M. Rusanen, P. Raybaud, S. Kasztelan, P. da Silva, H. Toulhoat, J. Catal., 2009, **267**, 67-77.
13. H. Aritani, T. Tanaka, T. Funabiki, S. Yoshida, K. Eda, N. Sotani, M. Kudo, S. Hasegawa, J. Phys. Chem., 1996, **100**, 19495-19501.
14. H. Aritani, O. Fukud, A. Miyaji, S. Hasegawa, Appl. Surf. Sci., 2001, **180**, 261-269.
15. Y.V. Zubavichus, A.S. Golub, Y.N. Novikov, Y.L. Slovokhotov, A.N. Nesmeyanov, P.J. Schilling, R.C. Tittsworth, J. Phys. IV, 1997, **7**, 1057-1059.
16. Robert G Mortimer, Physical chemistry, San Diego: Harcourt/Academic Press, ©2000, 2nd ed.
17. R.S. Smart, W.M. Skinner, A.R. Gerson, Surf. Interface Anal., 1999, **28**, 101-105.
18. X.S. Li, Q. Xin, X.X. Guo, P. Grange, B. Delmon, J. Catal., 1992, **137**, 385-393.
19. A.K. Datye, S. Srinivasan, L.F. Allard, C.H.F. Peden, J.R. Brenner, L.T. Thompson, J. Catal., 1996, **158**, 205-216.
20. E. Devers, P. Afanasiev, B. Jouguet, M. Vrinat, Catal. Lett., 2002, **82**, 13-17.
21. G. Alonso, G. Berhault, A. Aguilar, V. Collins, C. Ornelas, S. Fuentes, R.R. Chianelli, J. Catal., 2002, **208**, 359-369.
22. M. Vrinat, M. Breysse, C. Geantet, J. Ramirez, F. Massoth, Catal. Lett., 1994, **26**, 25-35.

 